One-Pot Synthesis of Aminated Bimodal Mesoporous Silica Nanoparticles as Silver-Embedded Antibacterial Nanocarrier and CO_2 Capture Sorbent

Yun Li,[1] *Amit Kumar Tiwari*,[1,⊥] *Jingyi Sandy Ng*,[1] *Geok Leng Seah*,[1] *Hong Kit Lim*,[1] *Teeraporn Suteewong*,[2] *Chor Yong Tay*,[1] *Yeng Ming Lam*,[1] and *Kwan W. Tan*[1,*]

[1]School of Materials Science and Engineering, Nanyang Technological University, Singapore 639798, Singapore.

Email: kwtan@ntu.edu.sg

[2]Department of Chemical Engineering, School of Engineering, King Mongkut's Institute of Technology Ladkrabang, Bangkok 10520, Thailand.

[⊥]Present Address: Department of Chemistry, School of Advanced Sciences, Vellore Institute of Technology-Vellore, Tamil Nadu, 632014, India.

Keywords: self-assembly, mesoporous, bimodal, Gemini surfactant, silica, antimicrobial, CO_2 capture

Abstract

Mesoporous silica nanoparticles have highly versatile structural properties that are suitable for a plethora of applications including catalysis, separation and nanotherapeutics. We report a one-pot synthesis strategy that generates bimodal mesoporous silica nanoparticles via co-assembly of a structure-directing Gemini surfactant ($C_{16\text{-}3\text{-}16}$) with tetraethoxysilane/(3-aminopropyl)triethoxysilane-derived sol additive. Synthesis temperature enables control of the nanoparticle shape, structure and mesopore architecture. Variations of the aminosilane/alkylsilane molar ratio further enables programmable adjustments of hollow to core-shell and dense nanoparticle morphologies, bimodal pore sizes and surface chemistry. The resultant Gemini-directed aminated mesoporous silica nanoparticles have excellent carbon dioxide adsorption capacities and antimicrobial properties against *E. coli*. Our results provide enhanced understandings in the structure formation of multiscale mesoporous inorganic materials that are desirable for numerous applications such as carbon sequestration, water remediation and biomedical-related applications.

1. Introduction

Mesoporous inorganic materials with ordered architectures, high surface area and pore volume, tailorable pore size and pore size distribution, tunable composition and surface chemistry, have stimulated widespread interests for various applications[1] ranging from catalysis,[2,3] separation,[4,5] optics,[6] energy generation and storage,[7–11] biomedical,[12–17] farming[18] and semiconductor nanostructures.[19–21] Mesoporous silica materials are especially well-explored as a model system for sol-gel chemistry[22,23] and are known for its versatility to generate periodic/quasicrystalline nanoarchitectures and pore geometries in various macroscopic forms (e.g., nanoparticles, films, monoliths),[24–41] as well as serving as nanocasting templates to access other functional materials.[20,42,43] Owing to all these structural features, mesoporous silica nanoparticles (MSNs) are highly sought after in drug delivery, diagnostics and sensing applications.[12–16,34]

Conventional MSNs generated from self-assembling mixtures of organic structure agents (e.g., surfactants, block copolymers) and silica sol precursors typically have a single type ordered/disordered mesostructure with monomodal pore size and narrow pore size distribution.[44] Extending the control of MSN shape and structure, pore size and pore geometry as well as surface chemistry enable further broadening of functionality and application space.[45] For example, multicompartment MSNs with different cubic and/or hexagonal-arranged mesopore compartments impart multifunctionalities and individual stimulated responses;[32,46] however, the pore sizes of such multicompartment MSNs are usually less than 10 nm, constraining the size of adsorbate materials and effective mass transfer.[47] Hierarchical MSNs with bimodal pore sizes (<5 and 20–50 nm) have been reported,[47–52] but the synthesis protocols either involve many steps,[47,51,52] require multiple structure-directing agents,[49,50] or the macroscopic form is that of a

typical sphere shape that poses limits in transport and adhesion properties and surface interactions.[48,53,54] A facile one-pot method was described by Yan and co-workers[16] mixing cetyltrimethylammonium bromide (CTAB) surfactant with tetraethoxysilane (TEOS) and (3-aminopropyl)triethoxysilane (APTES) as silica co-precursors to form hollow MSNs. However, the silica mesostructure order and pore geometry characteristics were not fully defined and the control of MSN shape and pore size was not established.[16]

Here, we describe a facile one-pot synthesis approach mixing a structure-directing Gemini diammonium surfactant ($C_{16}H_{33}(CH_3)_2NBr–C_3H_6–NBr(CH_3)_2C_{16}H_{33}$, $C_{16\text{-}3\text{-}16}$) with TEOS to generate hollow MSNs with tunable nanoparticle (NP) shapes (sphere, biconcave and cube), variable pore architectures (lamellar and cylinder) and bimodal mesopore sizes under different temperatures. Adding APTESas a co-precursor provides a simple lever to modify the MSN size (~100 to 250 nm) and NP structure (hollow, dense, core shell) as well as functionalize the MSN surface with primary amine groups. A nonclassical formation mechanism based on the oriented aggregation of structured Gemini/silica hybrid clusters is proposed. The resultant aminated bimodal MSNs serve as a suitable nanocarrier platform to host metallic silver (Ag) with controlled ion release rates to promote antibacterial activities as well as a solid-state sorbent with high carbon dioxide (CO_2) adsorption capacities and stable cyclability.

2. Results and Discussion

2.1. Co-Assembly of $C_{16\text{-}3\text{-}16}$ Gemini Surfactant and TEOS-Derived Silica

Gemini surfactants, made up of two charged polar head groups separated by a methylene spacer and with each head group attached to a hydrocarbon tail, readily transform into lyotropic/thermotropic liquid crystalline structures.[26,55,56] The structure-directing agent in this study, $C_{16\text{-}3\text{-}16}$, is a Gemini surfactant with C_{16} tails and a C_3 spacer separating the quaternary nitrogen atoms. It was reported that $C_{16\text{-}3\text{-}16}$ micelles in aqueous solutions (2.5 to 10 mM) exhibited disklike shape at lower temperatures (~30 °C) and elongated rod shape at higher temperatures (40 to 70 °C).[57] We expected $C_{16\text{-}3\text{-}16}$ to form similar shaped micelles in the mixed solvent of deionized water and ethanol (EtOH, 3.6 mM). In the present work, TEOS was added as a silica precursor into the Gemini surfactant solution (4 mM) under basic conditions, forming bimodal MSNs (BMSNs) of various shapes and structures at temperatures of 30 to 95 °C. Transmission electron micrographs (TEM) in Figure 1 demonstrate the critical role of synthesis temperature in the shape and structure transitions of Gemini-directed BMSNs after surfactant removal by acid extraction.

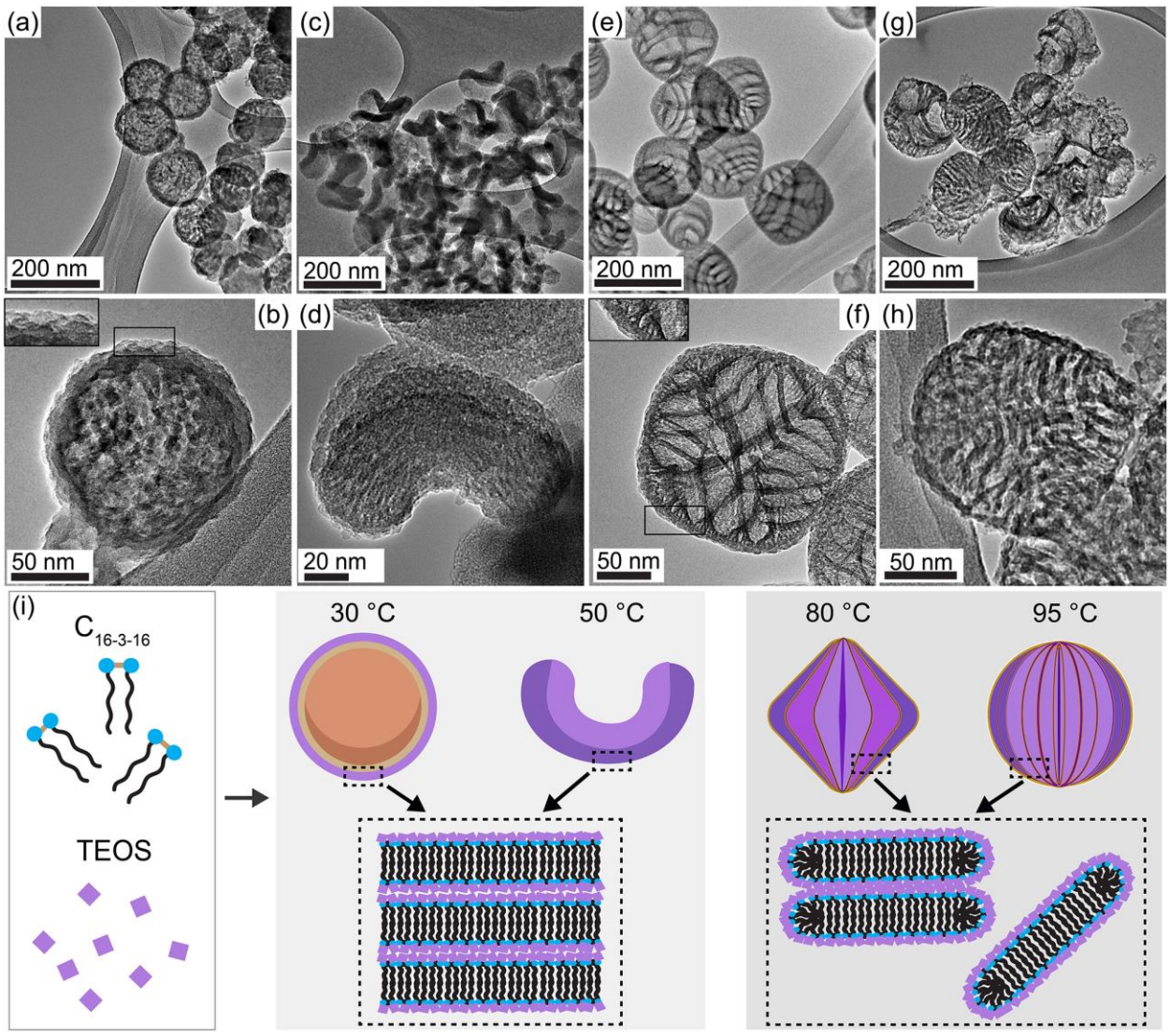

Figure 1. (a–h) TEM micrographs and (i) schematic representations of BMSNs generated by co-assembly of $C_{16\text{-}3\text{-}16}$ and TEOS-derived sol additive at 30 ° C (a,b), 50 ° C (c,d), 80 ° C (e,f) and 95 ° C (g,h), after surfactant removal. Insets in (b) and (f) show the surface morphologies of the selected regions at higher magnifications.

Figure 1a,b shows that BMSNs synthesized at 30 °C were spherical in shape with a hollow particle structure and diameters ranging from 110 to 140 nm. Closer TEM examination of Figure 1b suggests the rough NP surface was composed of non-uniformly stacked layers of silica

likely due to the incomplete condensation of TEOS.[58] Interestingly, TEM in Figure 1c,d show the cross-section view of BMSNs of 50 °C with a new biconcave disk shape and similar NP sizes of 110 to 130 nm. The BMSN biconcave disks were made up of more regularly stacked layers of silica nanosheets (Figure 1d) relative to the 30 °C-sample, attributed to faster silica condensation rates and improved self-organization process at 50 °C.[58] Scanning electron micrographs (SEM) in Figure S2a,b corroborated the particle morphology of TEOS-derived BMSNs of 30 and 50 °C at lower magnifications.

Higher synthesis temperatures of 80 and 95 °C promoted formation of alternative cubic and spherical shaped hollow BMSNs, respectively, decorated with distinctive surface wrinkles (Figure 1e–h). Resultant cubic BMSNs of 80 °C were well-defined with relatively uniform average size of 170 nm (Figure 1e and 2a), whereas collapsed BMSNs and particle aggregations were more prevalent at 95 °C (Figure 1g). Moreover, surface wrinkles on the 80 °C-BMSNs appeared more well-spaced compared to the randomly dense-packed wrinkles on the 95 °C-BMSNs (compare Figure 1f and h). The regularly spaced surface wrinkles and cubic shape of the 80 °C-BMSNs are similarly observed in SEM (Figure S2c). Importantly, higher magnification TEM reveals the silica mesopore channels were oriented radially from the particle core (Figure 1f).

We performed nitrogen sorption measurements to evaluate the bimodal porosity characteristics of TEOS-derived BMSNs. Nitrogen sorption isotherms displayed in Figure 3b,c and S3 indicated a large increase in BET surface areas from ~80 m^2/g to 300 m^2/g as the synthesis temperatures were raised from 30 to 80 °C (Table S1), consistent with structural evolution toward the cubic hollow particle morphology. Moreover, the BJH pore size distribution

plots in Figure 3c and S3 revealed the bimodal pore sizes reduced from ~10–70 nm to ~3–60 nm for BMSN samples of 50 and 80 °C, respectively.

The thermotropic BMSN mesophase formation is likely a result of the Gemini surfactant micelle shape and electrostatic interactions between the surfactant ammonium headgroups with silica sol oligomers. We postulate that $C_{16\text{-}3\text{-}16}$ surfactants formed disk-like mesophases in the mixed water/EtOH solvent at lower temperatures (⩽50 °C).[56,57] The base-catalyzed TEOS-derived silica oligomers were negatively-charged and attracted to the disk-like cationic Gemini micelles, promoting self-assembly into an organic-inorganic lamellar phase (see schematic in the second panel of Figure 1i).[54,59] At 30 °C, the lamellar phase further evolved into spherical-shaped multilamellar vesicles to minimize excess surface energy.[50] Acetic acid treatment to remove $C_{16\text{-}3\text{-}16}$ resulted in multi-shell hollow particles (Figure 1b). The higher temperature of 50 °C varied the charge density of silica oligomers due to slightly increased TEOS hydrolysis/condensation rates,[26,58] yielding biconcave shaped particles with multistacked silica mesostructure after surfactant removal (Figure 1d).[50]

At even higher temperatures (>50 °C), the Gemini surfactant micelle assumed an elongated rod-like shape.[56,57] In addition, the hydrolysis and condensation reactions of TEOS further accelerated, resulting in more complex interactions between elongated rod-like $C_{16\text{-}3\text{-}16}$ micelles with the hastily formed silica oligomers and self-assembled into the disordered cylindrical mesophase (see schematic in the third panel of Figure 1i).[54,57,59] We speculate the synthesis temperature of 80 °C provide the optimal control of thermodynamic and kinetic self-assembly driving forces to form well-defined cubic-shaped hollow BMSNs with radial mesopore channels (Figure 1f). Synthesis at 95 °C confirmed this hypothesis as ruptured MSNs and

particle aggregation were observed (Figure 1g), attributed to overly rapid hydrolysis and condensation reactions of TEOS, resulting in irregularly sized surfactant/silica nanoclusters that disrupted the self-assembly process.[33,58]

2.2. Influence of APTES/TEOS Ratios on Gemini-Directed BMSNs

Aminosilanes are well-explored in the synthesis of MSNs either as a co-structure directing agent,[60,61] a co-condensing silica precursor[13,32,34,46] or to introduce chemical functional groups on the MSN surface.[13,16,33] We introduced APTES as a co-structure director and co-condensing silica precursor to further tune the shape, size and mesophase of Gemini-directed BMSNs in the one-pot synthesis protocol. TEM in Figure 2 shows the structural evolution of aminated BMSNs with increasing molar ratios of APTES-to-TEOS at 80 °C with a constant silane concentration of 4 mM, while keeping all conditions the same. Aminated BMSNs are designated as *X*-NH_2-BMSNs where *X* denotes the APTES molar percentage (0–50 mol %).

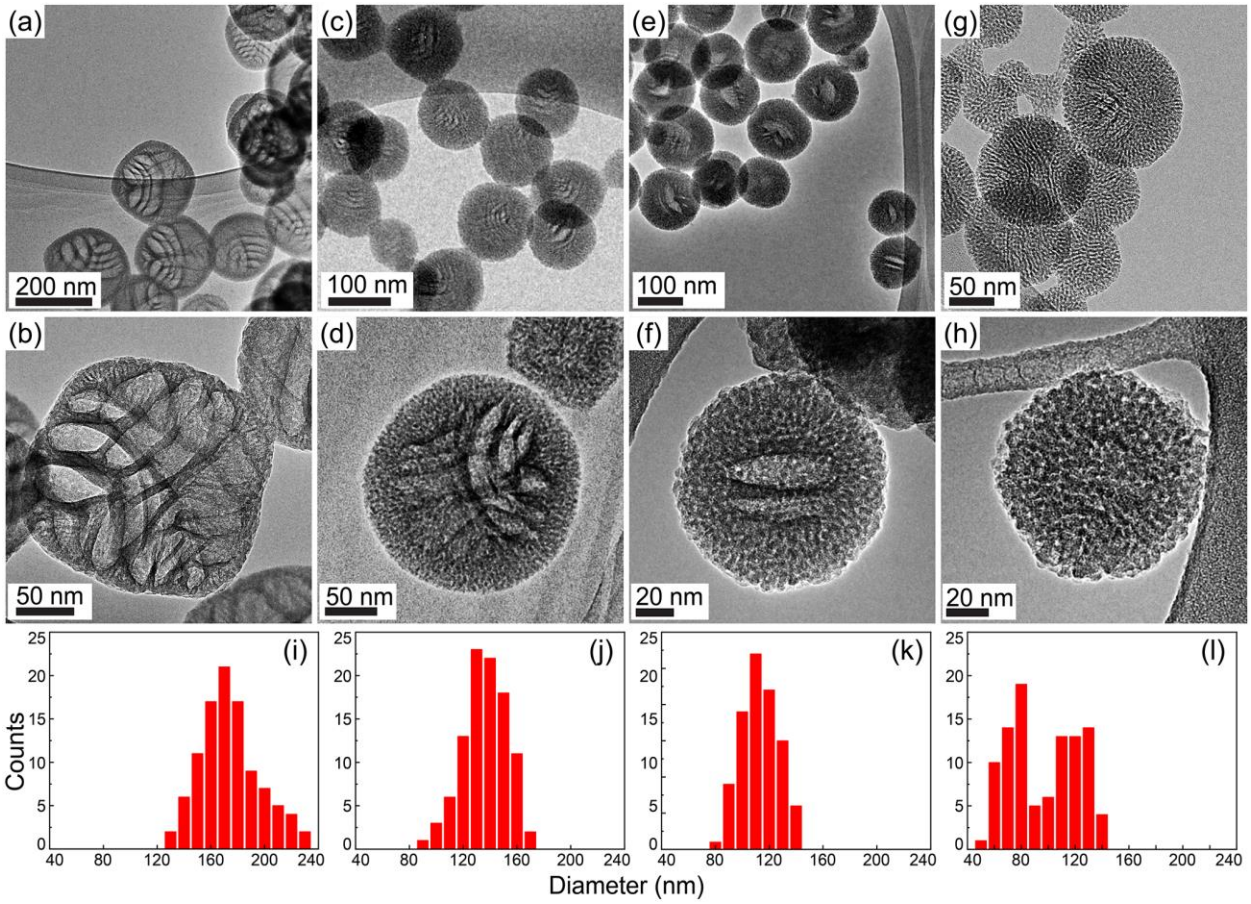

Figure 2. (a–h) TEM micrographs and (i–j) corresponding particle size histograms of NH_2-BMSNs with increasing APTES concentrations of 0 mol % (a,b,i), 10 mol % (c,d,j), 20 mol % (e,f,k) and 30 mol % (g,h,l), synthesized at 80 °C, after surfactant removal.

Figure 2 a,b,i shows cubic-shaped hollow BMSNs with an average diameter of ~180 nm when no APTES was added as described earlier (0-NH_2-BMSNs, see also Figure 1e,f). With 10 mol % APTES as co-precursor, the first TEM observations made were that the aminated BMSNs were round and smaller in size (10-NH_2-BMSNs, Figure 2c,d). The particle size and size distribution improved to an average diameter of around 140 nm (Figure 2j). However, the particle shell thickness and mesoporous silica structure disorder also clearly increased. Further increase in APTES concentrations resulted in even smaller particles, approximately 120 and 90

nm for 20-NH_2-BMSNs and 30-NH_2-BMSNs (Figure 2k, l), respectively, as well as the densification of NH_2-BMSNs as reflected by increased darker contrast in the particle center regions under bright-field TEM (Figure 2e–h). All the evidence suggests the structure evolution from the outer to the inner portion of the NPs with increasing amounts of APTES that engulfed the hollow interior. The decrease in particle size and size distributions of NH_2-BMSNs were corroborated by dynamic light scattering measurements (Figure S4). However, further increase in APTES up to 50 mol % resulted in amplified occurrences of aggregation of irregularly shaped NH_2-BMSNs depicted in Figure S5.

Small-angle X-ray scattering (SAXS) plots in Figure 3a depict the structural evolution of NH_2-BMSNs with increasing APTES-to-TEOS molar ratios before (dashed curves) and after surfactant removal (solid curves) as a collective average. For pure TEOS-derived particles, the SAXS pattern of as-made 0-NH_2-BMSNs (dashed black curve) displays only a single principal peak at $q^* = 1.88\ nm^{-1}$, consistent with the disordered cylindrical morphology observed in TEM (Figure 1f, 2b). Interestingly, there is a significant drop in peak intensity after Gemini surfactant removal (solid black curve), attributed to the reduced structural integrity of the hollow particle. The shift of the principal reflection to a smaller angular position is likely an artefact due to the substantial peak broadening event. As APTES concentrations increased up to 30 mol%, we observed a blue shift in the angular positions and broadening of the principal SAXS peaks for both as-made and surfactant-free NH_2-BMSNs (Table S1). This corresponds to larger *d*-spacing values for the NH_2-BMSNs from 3.3 nm (0-NH_2-BMSNs) to 4.7 nm (30-NH_2-BMSNs). The intensities of the principal SAXS reflections remained almost unchanged for both as-made and surfactant-free TEOS/APTES-derived NH_2-BMSNs, indicating improved particle structural integrity with the addition of APTES (compare red, green and blue-colored dashed and solid

curves). We further note the broader SAXS principal reflections of NH_2-BMSNs were consistent with the 3-dimensional (3D) disordered wormhole-like mesostructure as observed in TEM (Figure 2c–h).

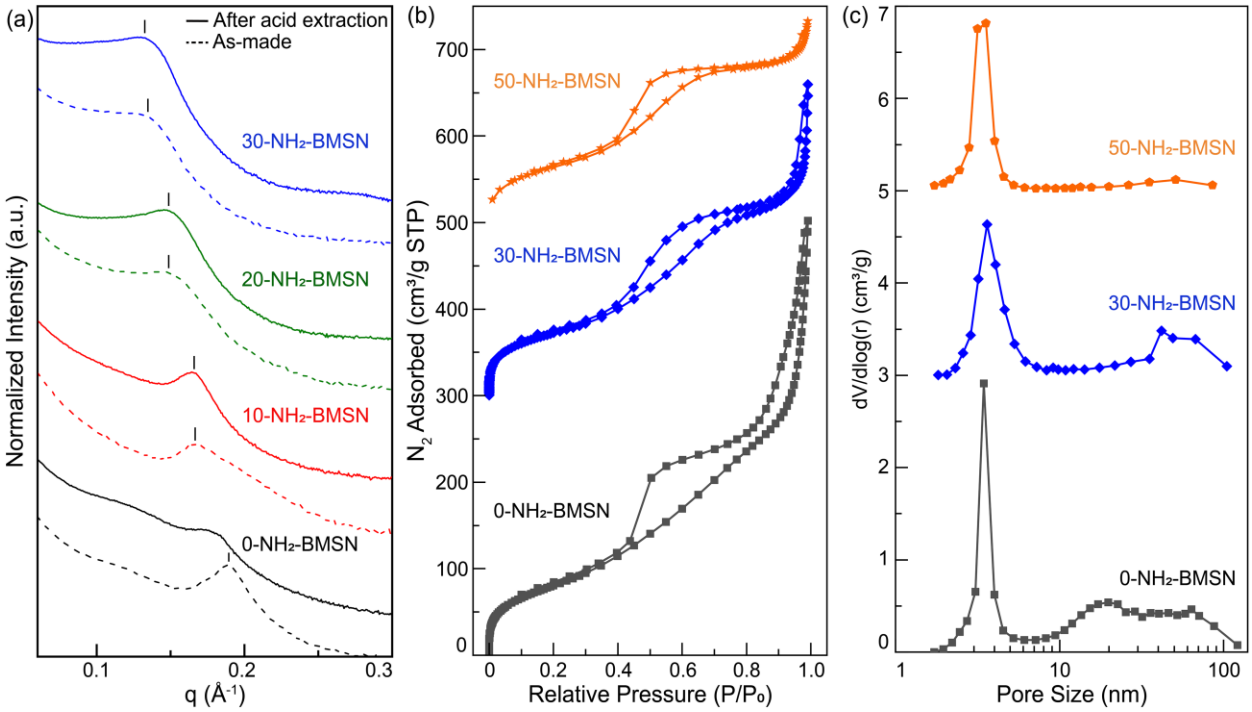

Figure 3. (a) SAXS patterns of NH_2-BMSN samples synthesized at 80 °C before (dashed lines) and after surfactant removal by acid extraction (solid lines). Tick marks in (a) indicate the respective principal SAXS reflections. (b) Nitrogen sorption isotherms and (c) BJH pore size distributions of surfactant-free NH_2-BMSN samples. Data were offset vertically for the isotherms (by 300 and 500 cm^3/g for 30-NH_2-BMSNs and 50-NH_2-BMSNs, respectively) and BJH pore size distribution plots (by 3 and 5 $cm^3/g\cdot$for 30-NH_2-BMSNs and 50-NH_2-BMSNs, respectively) to improve clarity.

Nitrogen sorption analysis of surfactant-free NH_2-BMSNs corroborated TEM and SAXS data. Figure 3b and S6 shows that the nitrogen sorption isotherms of 0-NH_2-BMSN, 20-NH_2-

BMSN, 30-NH_2-BMSN and 50-NH_2-BMSN are of type IV with some hysteresis. BET surface areas and pore volumes decreased from 300 to 180 m^2/g and 0.72 to 0.24 cm^3/g, respectively, as APTES concentrations increased from 0 to 50 mol % (see Table S1). The decreasing porosity values are consistent with the particle morphology change from hollow-type to dense BMSN particles.

The BJH pore size distribution plot of 0-NH_2-BMSN sample in Figure 3c (black curve) shows a bimodal pore size distribution with an intense peak centered at ~3.46 nm and a significant population of pores between 10 to 100 nm represented by the area under the secondary peak. The BJH mesopore size is close to the TEM observations of ~2–2.4 nm (Figure S7). For the 30-NH_2-BMSN sample, the wormhole-like mesopore size remained almost constant at ~3.5 nm, while the population of larger pores of 40–60 nm reduced substantially, consistent with the densification of NH_2-BMSNs. For the 50-NH_2-BMSN sample, the wormhole-like mesopore of 3.6 nm is the most dominant in the BJH pore size distribution plot, suggesting an almost completely dense mesoporous silica nanoparticle. Capillary condensation of liquid nitrogen at ~0.4P/P_0 observed in all of the isotherms shown in Figure 3b corroborated the consistent mesopore size of 3.6 nm for the NH_2-BMSNs.

We performed Fourier transform infrared (FTIR) spectroscopy to estimate the amount of amine functional groups present in the NH_2-BMSNs samples as shown in Figure S8a. FTIR spectrum of the control 0-NH_2-BMSN sample exhibits the highest intensity peaks at 1087 and 3450 cm^{-1}, corresponding to Si–O–Si and SiO–H bond vibrations, respectively. These signal intensities decreased gradually as observed in the FTIR spectra of NH_2-BMSNs with higher amounts of APTES appended. Instead, new IR peaks appeared at the 1560 and 3000–3300 cm^{-1} bands, attributed to N–H bending and primary amine stretching vibrations, respectively. Figure

S8b shows the plot of peak intensity ratios of N–H bonds (1560 cm^{-1}) relative to Si–O–Si bonds (1087 cm^{-1}) as a function of initial APTES loading concentrations, providing a semiquantitative affirmation of amine functional groups present in the NH_2-BMSNs.

The formation and cooperative self-assembly of periodic silica mesostructures is regulated by the complex interactions between structure-directing ionic surfactants (S) and silicate additive (I), especially on the organic/inorganic interfaces.[62,63] The synthetic route in the self-assembly of cationic $C_{16\text{-}3\text{-}16}$ Gemini surfactant (S^+) and TEOS-derived silicate oligomers (I^-) under basic conditions can be described by the matching of S^+I^- via attractive electrostatic Coulomb force.[62,63] The addition of aminosilane promotes further interactions between the charged species and enables mediation of surfactant micelle geometry and packing behaviors as co-structure-directing agent and co-condensing silicate additive as well as to slow down sol–gel condensation reactions.[31–35,60,64,65] For example, Garcia-Bennett and co-workers reported the influence of pH of the synthesis solution on aminosilane precursors and MSN formation.[60] For pH values above the pK_a of APTES (>10.6), the amine groups became deprotonated (N^0) and allowed the hydrophobic components of APTES to penetrate into the hydrophobic micelle core of the cetyltriethylammonium bromide surfactant (denoted as the $S^+{\sim}N^0I^-$ route), altering the micelle curvature and resultant mesophase morphologies.[60] We postulate a similar formation mechanism for the growth of Gemini-directed NH_2-BMSNs at 80 °C as shown schematically in Figure S9.

The pH in our synthesis solution environment was ~11 using sodium hydroxide (NaOH) as base catalyst for the sol–gel reactions. Silicate oligomers derived from the rapid hydrolysis and condensation reactions of TEOS were attracted to the ammonium headgroups of rod-like $C_{16\text{-}3\text{-}16}$ micelles via the S^+I^- pathway,[57] resulting in the nucleation of radially oriented disordered

cylinders on the surface of cubic-shaped hollow BMSNs (vide supra, see Figure 2b and S9). The addition of APTES induced new changes in hydrolysis and condensation rates of silicate oligomers and nucleation of BMSNs.[33,60] Firstly, most of the amino groups of APTES were expected to be in the neutral state, enabling the intercalation of aminopropyl medieties in the hydrophobic Gemini surfactant micelle cores and thereby induced further micelle shape change toward the wormhole-like mesostructure (Figure S9). Secondly, APTES likely promoted the formation of small silica clusters of various sizes with the 3D disordered wormhole-like morphology.[33] These similarly structured surfactant/silica clusters then packed together, growing into spherical hollow particles with thicker shells of wormhole-like structured mesoporous silica (Figure 2d). Thirdly, further increase in APTES enabled even slower condensation rates that promoted denser packing of the structured hybrid clusters, generating mesoporous silica particles with smaller hollow cores (Figure 2f, h). As more silica building blocks were consumed to form dense particles at higher APTES concentrations, the size of resultant MSNs became progressively smaller (compare Figure 2h and 2a). This is corroborated by the increased silica wall thicknesses obtained from nitrogen sorption measurements as BJH mesopore diameters remained unchanged (see Figure 3c and Table S1). The proposed mechanism is similar to the non-classical growth of mesocrystals that was observed in the formation of well-ordered aminated CTAB-directed MSNs via organization of mesostructured silica clusters.[33,66]

2.3. BMSN Silver-Embedded Nanocarrier and CO_2 Sorbent Applications

Gemini-directed self-assembly provides a one-pot approach to synthesize BMSNs with control of high surface area and accessibility, pore geometry and size, and active amine functional groups desirable for many applications. In particular, NH_2-BMSNs with different bimodal pore sizes could potentially control the release of metal ions to enable high antimicrobial

efficiencies.[67] We performed $AgNO_3$ backfilling experiments with the 0-NH_2-BMSN and 20-NH_2-BMSN samples, followed by heating at 100 °C to induce amine-assisted $AgNO_3$ reduction into Ag NPs in the hollow mesoporous silica particles.[68,69] TEM image in Figure 4a shows sub-10-nm $AgNO_3$ particles scattered randomly on the bare silica NPs (0-NH_2-BMSN), attributed to poor adhesion and loss of salt through larger pores. Contrarywise, TEM in Figure 4b shows the successful growth of Ag NPs with diameters of 20 to 50 nm in the hollow cores of aminated silica NPs (20-NH_2-BMSN), attributed to chemical reduction of $AgNO_3$ by the amine-functionalized surface.[68,69] Confinement of Ag NPs in 20-NH_2-BMSNs was confirmed via TEM inspection of a series of images taken at different rotation angles (Figure S10), energy dispersive X-ray spectroscopy (EDS) mapping analysis (Figure S11) and wide-angle X-ray scattering (Figure S12). The 20-NH_2-BMSNs with a smaller hollow core and thicker mesostructured silica shell has the optimal nanocarrier design to store and slowly release Ag^+ ions to inhibit bacterial activities.

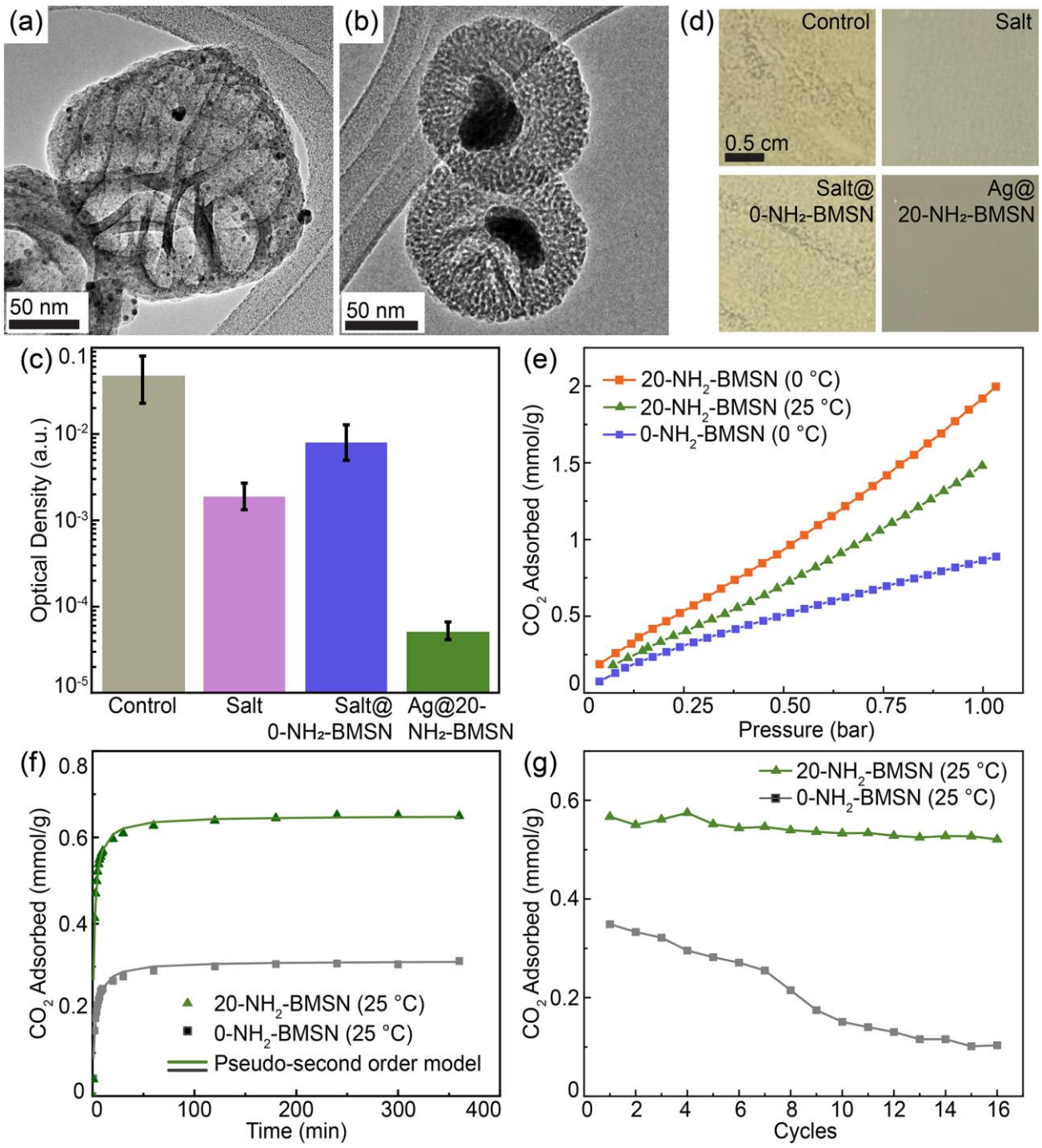

Figure 4. TEM images of (a) $AgNO_3$@0-NH_2-BMSNs and (b) Ag@20-NH_2-BMSNs after backfilling experiments. (c) OD measurements of *E. coli* growth in LB broths that contained no medium (control), $AgNO_3$ salt, $AgNO_3$@0-NH_2-BMSNs and Ag@20-NH_2-BMSNs. (d) Optical images of *E. coli* colonies in agar plates streaked with bacterial cultures that contained no

medium (control), $AgNO_3$ salt, $AgNO_3$@0- NH_2-BMSNs and Ag@20-NH_2-BMSNs, after incubation for 24 h at 37 °C. (e) CO_2 adsorption isotherms of 0-NH_2-BMSNs and 20-NH_2-BMSNs at 0 °C and 25 °C for 1 bar. (f) CO_2 adsorption isotherm plots of 0-NH_2-BMSNs and 20-NH_2-BMSNs and respective fitted curves from the pseudo-second order kinetic model, as well as (g) cyclic CO_2 adsorption capacity plots of 0-NH_2-BMSNs and 20-NH_2-BMSNs, all measured by the TGA method at 25 °C.

To evaluate antibacterial performance, we immersed samples of $AgNO_3$ salt, $AgNO_3$@0-NH_2-BMSN and Ag@20-NH_2-BMSN in Escherichia coli (*E. coli*) cultures and incubated at 37 °C for 24 h. A suspension of *E. coli* with no medium was studied as the control for comparison. The optical density (OD) measurement bar chart in Figure 4c indicates the Ag@20-NH_2-BMSN sample exhibited the most efficient suppression of *E. coli* activities after incubation at 37 °C for 24 h, followed by the pure $AgNO_3$ salt. We hypothesize the hollow Ag@20-NH_2-BMSN sample provided a more controlled and sustained cargo release of Ag^+ ions through the mesopores, inhibiting bacterial growth via rupture of the *E. coli* cell membranes.[67] This was supported by the speciation measurements of Ag^+ ions discharged by Ag@20-NH_2-BSMN using an inductively coupled plasma optical emission spectrometer (ICP-OES) over a 24 h period (Figure S13). This was further corroborated by the agar streak plate method that showed negligible *E. coli* bacterial activity in the Ag@20-NH_2-BMSN sample (Figure 4d and S14). We could further control the Ag^+ release rates to enhance antibacterial performance by tuning the surface silica mesopore size. For instance, adding hydrophobic pore expanders into the self-assembling mixtures would result in larger pores,[28] while employing Gemini surfactants with shorter alkyl tails would reduce the mesopore size.[26]

Ordered mesoporous inorganic materials are well-explored as potential solid-state adsorbents for post-combustion CO_2 capture (see Table S2).[5,70] For example, Fan and co-workers synthesized SBA-15 mesoporous silica platelets, followed by grating aminosilanes on the silica surface by a post-process wet impregnation step.[70] The resultant 3-aminopropyltrimethoxysilane-grafted SBA-15 platelets exhibited a CO_2 adsorption capacity of 1.58 mmol/g at 25 °C for 1 bar. It is, however, more advantageous to synthesize animated mesoporous silica adsorbents through the simpler one-pot approach. We demonstrated the NH_2-BMSN sample series as a suitable solid-state adsorbent candidate for CO_2 capture. Figure 4e shows the CO_2 adsorption isotherms of bimodal mesoporous nanoparticles of pure silica (0-NH_2-BMSN) and amine-functionalized silica (20-NH_2-BMSN) samples. At 0 °C for 1 bar, 20-NH_2-BMSN has a CO_2 absorption capacity of 2.00 mmol/g that is more than 2 times the pure silica sample (0.89 mmol/g), attributed to the strong chemical affinity of CO_2 molecules to the primary amine surface groups. The CO_2 adsorption capacity of 20-NH_2-BMSN at 25 °C remained excellent at 1.48 mmol/g for 1 bar. From the Clausius−Clapeyron equation, the isosteric heat of adsorption for CO_2 in 20-NH_2-BMSNs was estimated to range from ~19.4 kJ/mol (at 0.2 mmol/g) to ~6.4 kJ/mol (at 1.5 mmol/g), as shown in Figure S15.[70,71]

We assessed the CO_2 adsorption behaviors of Gemini-directed BMSNs using the thermogravimetric analysis (TGA) method at 25 °C. Figure 4f shows that both 0-NH_2-BMSN and amine-functionalized 20-NH_2-BMSN samples reached their near-saturation CO_2 capacities of ~0.30 and 0.63 mmol/g, respectively, within 30 min. The TGA-based CO_2 isotherms were further evaluated with three kinetic models: the pseudo-first order, the pseudo-second order and the Arvrami's fraction-order models.[72,73] From linear regression analysis, we obtained the respective kinetic rate constants and squared correlation coefficient (R^2) values summarized in

Table S3. The pseudo-second order kinetic model provided the best fit to the TGA-derived CO_2 isotherms as shown in Figure 4f. The pseudo-second order rate constant values (k_2) for CO_2 adsorption by both 0-NH_2-BMSN (k_2 = 1.249 min^{-1}) and 20-NH_2-BMSN (k_2 = 1.099 min^{-1}) are very similar. Finally, the amine-functionalized 20-NH_2-BMSN sample exhibited a highly stable CO_2 adsorption capacity of 0.55 mmol/g after 16 TGA cycles, whereas the TEOS-derived 0-NH_2-BMSN retained only a third of the original CO_2 adsorption capacity (0.12 versus 0.35 mmol/g).

3. Conclusions

We have demonstrated a facile one-pot synthesis protocol to synthesize well-defined amine-functionalized mesoporous silica nanoparticles via co-assembly of a Gemini surfactant ($C_{16\text{-}3\text{-}16}$) as structure-directing agent and co-condensing TEOS and APTES-derived silica sol precursors. Synthesis temperature provides a simple lever to vary the Gemini micelle shape and facilitates the formation of TEOS-derived mesoporous silica nanoparticles with different particle shapes and structures (sphere, biconcave disk, cube), silica mesostructures (lamellar and cylinders) and bimodal pore sizes. Mixing APTES with TEOS further enables variations of the Gemini micelle geometries and packing behaviors as well as silica condensation rates, thereby imparting control to form hollow, core-shell and dense mesoporous silica sphere nanoparticles with the alternative wormhole-like mesostructure. The aminated hollow bimodal MSNs were suitable nanocarriers of Ag NPs that allowed effective and sustained release of Ag^+ ions inhibiting *E. coli* growth. NH_2-BMSNs also showed enhanced CO_2 adsorption capacities and longer cyclability, attributed to the strong chemical affinity of CO_2 molecules to the amine

surface groups. We envisage the programmable one-pot strategy to synthesize variable functional MSNs with direct control of NP structures, shapes, morphologies and surface chemistries could push new frontiers in “smart” nanotechnology-enabled applications such as sensing, catalysis, nanomedicine and carbon sequestration.

4. Experimental Section

Materials. Tetraethoxysilane (TEOS, >98%), 1,3-dibromo propane and *N*,*N*-dimethylhexadecylamine were obtained from TCI Chemicals. (3-aminopropyl)triethoxysilane (APTES, ⩾98%), NaOH (⩾97%, pellets) %) and silver nitrate ($AgNO_3$, ⩾99.0%) were purchased from Sigma Aldrich. 200-proof ethanol (EtOH) was purchased from Merck. All materials were used as obtained.

Synthesis of Gemini diammonium $C_{16\text{-}3\text{-}16}$ surfactant. The $C_{16}H_{33}(CH_3)_2NBr–C_3H_6–NBr(CH_3)_2C_{16}H_{33}$ ($C_{16\text{-}3\text{-}16}$) surfactant was prepared as reported elsewhere.[74] Briefly, 1, 3-dibromopropane was mixed with 2 molar equivalent (plus a 10% excess) of *N*,*N*-dimethylhexadecylamine. The mixture was refluxed in dry EtOH at ~80 °C for 72 h, followed by solvent extraction using a rotary evaporator. The solid residues were purified via recrystallization in ethyl acetate/methanol (10:1, v/v) several times and characterized by ^{1}H-NMR spectroscopy.

Synthesis of Gemini-directed BMSNs: MSN samples were synthesized using a modified procedure.[38] A clear solution of Gemini surfactant (0.148 g, 2×10^{-3} mol) in a mixed solvent of deionized water (38 g, 2.11 mol) and EtOH (13.8 g, 0.3 mol) was prepared in a round-bottom glass vessel, followed by the addition of 0.1 M NaOH (6.5 g) as base catalyst. TEOS (0.89 mL,

4×10^{-3} mol) was added into the clear solution and gently stirred at 30 °C for about 10 min. The reaction mixture with pH of ~11 was left undisturbed (no stirring) for another 48 h at 30 °C. After synthesis, the product mixture with pH of ~8–9 was neutralized with 0.1 M HCl. The Gemini surfactant/BMSN hybrid sample was then retrieved by centrifugation and rinsed in EtOH at least two times to remove excess surfactant and silica precursors. An EtOH/acetic acid mixture (95/5, v/v) was used to remove the surfactant by stirring for at least 30 minutes at room temperature, followed by centrifugation and rinsing in EtOH for at least two times. The BMSN synthetic procedure was repeated at higher temperatures of 50, 80 and 95 °C, respectively, under reflux. Unless otherwise stated, all BMSN samples were stored in the EtOH medium. For characterization, BMSN samples were rinsed in EtOH and dried overnight in a vacuum oven at room temperature.

Synthesis of NH_2-BMSNs: NH_2-BMSN samples were prepared at 80 °C using the same procedure as described above except for the use of mixed silane precursors. Varying amounts of TEOS and APTES but kept under the same concentration of 4 mM were added into the Gemini surfactant solutions, while all other chemicals were maintained constant.

Synthesis of Ag@NH_2-BMSNs: 20-NH_2-BMSNs (50 mg) sample was kept in a teflon-capped scintillation vial and degassed under vacuum overnight. A 2 ml ethanolic solution of $AgNO_3$ (0.05 M) was then slowly added into the vial using syringe with needle. The mixture was stirred at room temperature for 12 h (under cap), followed by stirring at 60 °C under ambient conditions (uncapped) until most of the solution evaporated. The composite sample was rinsed with EtOH 3 times to remove exceeding amounts of $AgNO_3$, followed by heating at 100 °C for 1 h to form the Ag@20-NH_2-BMSN sample via amine-assisted reduction.[69] The procedure was repeated for the 0-NH_2-BMSNs sample (50 mg).

Characterization: Small-angle X-ray scattering (SAXS) measurements were collected with a Xenocs Nano-inXider instrument using a Cu Kα radiation source and Dectris Pilatus 3 detectors. 2D SAXS patterns were azimuthally integrated around the beam center into 1D scattering intensity curves plotted against the scattering vector magnitude $q = 4\pi \sin \theta/\lambda$, where θ is half of the total scattering angle and λ is the X-ray wavelength. The d-spacing was calculated using $d = 2\pi/q^*$, where q^* is the scattering vector of the principal peak. Scanning electron micrographs (SEM) were obtained on Pt-coated MSN samples using a JEOL 7600F field-emission SEM equipped with a half-in-lens detector at 15 kV. Transmission electron micrographs (TEM) was obtained using a JEOL 2100F electron microscope with an operating accelerating voltage of 200 kV equipped a Gatan Ultrascan 1000XP CCD camera. Nitrogen sorption measurements were conducted using a Micromeritics ASAP 2020 system at −196 °C and analyzed with the BET (below 0.2 P/P_0) and BJH (desorption) models.[75,76] All samples were degassed at 130 °C overnight under vacuum before nitrogen sorption measurements.

Antibacterial Testing: An overnight culture of *E. coli* strain ATCC 25922 in Luria-Bertani (LB) broth was first prepared, following by dilution of the bacterial suspension 6 times and incubation at 37 °C for 3 h to enable logarithmic growth. Further dilution was performed to reach approximately 5×10^5 CFU/ml in 2 ml of LB broth contained in round-bottomed polypropylene test tubes (14 mm) (Greiner Bio-One®). Samples of $AgNO_3$ salt (0.05 M in EtOH), $AgNO_3$@0-NH_2-BMSNs (50 mg) and Ag@20-NH_2-20-BMSNs (50 mg) were then added into the test tubes. An *E. coli* LB broth suspension test tube with no medium (bare) was investigated as control sample. The test tubes were incubated under agitation at 37 °C for 24 h for bacteria growth. Turbidity measurements of *E. coli* cultures were obtained by optical density (OD) method using a spectrophotometer at the 600 nm wavelength. First measurements were obtained before

incubation to determine the appropriate dilution factor for the bacteria culture. Second measurements were obtained after incubation to determine the bacterial densities in the control and sample test tubes. The contents in the tubes were further diluted 1000 times and streaked onto LB agar plates for incubation at 37 °C for 24 h under static condition. Optical images of the respective LB agar streak plates were obtained with a digital camera.

Speciation analysis of Ag^+ released by Ag@20-NH_2-BMSN sample: A 25 mg/ml mixture of Ag@20-NH2-BMSN in deionized water was prepared in an Eppendorf tube and incubated at 37 °C under static conditions. At a specific time point during the total duration of 24 h, the mixture was first centrifuged at 10000 rpm for 3 min, followed by extraction of an aliquot containing 0.2 ml of the supernatant. The aliquot was further diluted 50 times with deionized water for speciation analysis. Separately, 0.2 ml of deionized water was added back into the mother mixture to replenish the sampling volume. The Ag^+ concentrations of the respective aliquots were analyzed using an inductively coupled plasma optical emission spectrometer (Avio 200 ICP-OES, PerkinElmer).

CO_2 Adsorption Measurements: CO_2 adsorption measurements based on the volumetric method were conducted using a Micromeritics ASAP2020 system at 0 and 25 °C. Samples were degassed at 130 °C overnight under vacuum before measurements. The density of carbon dioxide at 0 and 25 °C are 1.951 and 1.784 kg/m^3, respectively. For the TGA method, samples were loaded in a thermogravimetric analyzer (Thermal Analyzers Instrument 2950) for degassing at 100 °C for 6 h and subsequently cooled to 25 °C under a constant nitrogen flow of 60 cm^3/min. To obtain the CO_2 saturation adsorption capacities, the samples were loaded in a CO_2 environment under a constant CO_2 flow rate of 60 cm^3/min for 6 h at 25 °C.

A total of 16 CO_2 adsorption/desorption cycles were performed to evaluate the adsorption capacity retention properties of NH_2-BMSN samples. For the adsorption part of the first cycle, samples were loaded in a CO_2 environment at 25 °C under a constant CO_2 flow rate of 60 cm^3/min for 30 min, followed by desorption in a nitrogen environment at 120 °C for 30 min under a constant nitrogen flow rate flow rate of 60 cm^3/min. The samples were then cooled to 25 °C under nitrogen. The TGA-based CO_2 adsorption/desorption cycle was repeated for another fifteen times.

Supporting Information

The Supporting Information is available free of charge at https://pubs.acs.org/doi/

Additional characterization of BMSNs by NMR, DLS, TEM, EDS, WAXS, FTIR spectroscopy, ICP-OES, nitrogen sorption and antibacterial assays results.

Notes

The authors declare no competing financial interest.

Acknowledgements

This work was supported by a startup grant from Nanyang Technological University, Singapore. This work made use of research facilities at the Facility for Analysis, Characterization, Testing, and Simulation (FACTS), Nanyang Technological University, Singapore. The authors thank Y. Y. Tay for helpful experimental assistance and discussion.

References

(1) Davis, M. E. Ordered Porous Materials for Emerging Applications. *Nature* **2002**, *417* (6891), 813–821. https://doi.org/10.1038/nature00785.

(2) Taguchi, A.; Schüth, F. Ordered Mesoporous Materials in Catalysis. *Microporous Mesoporous Mater.* **2005**, *77* (1), 1–45. https://doi.org/10.1016/j.micromeso.2004.06.030.

(3) Li, Y.; Horia, R.; Tan, W. X.; Larbaram, N.; Sasangka, W. A.; Manalastas, W.; Madhavi, S.; Tan, K. W. Mesoporous Titanium Oxynitride Monoliths from Block Copolymer-Directed Self-Assembly of Metal–Urea Additives. *Langmuir* **2020**, *36* (36), 10803–10810. https://doi.org/10.1021/acs.langmuir.0c01729.

(4) Wu, Z.; Li, W.; Webley, P. A.; Zhao, D. General and Controllable Synthesis of Novel Mesoporous Magnetic Iron Oxide@Carbon Encapsulates for Efficient Arsenic Removal. *Adv. Mater.* **2012**, *24* (4), 485–491. https://doi.org/10.1002/adma.201103789.

(5) Seah, G. L.; Wang, L.; Tan, L. F.; Tipjanrawee, C.; Sasangka, W. A.; Usadi, A. K.; McConnachie, J. M.; Tan, K. W. Ordered Mesoporous Alumina with Tunable Morphologies and Pore Sizes for CO_2 Capture and Dye Separation. *ACS Appl. Mater. Interfaces* **2021**, *13* (30), 36117–36129. https://doi.org/10.1021/acsami.1c06151.

(6) Stefik, M.; Guldin, S.; Vignolini, S.; Wiesner, U.; Steiner, U. Block Copolymer Self-Assembly for Nanophotonics. *Chem. Soc. Rev.* **2015**, *44* (15), 5076–5091. https://doi.org/10.1039/C4CS00517A.

(7) Ji, X.; Lee, K. T.; Nazar, L. F. A Highly Ordered Nanostructured Carbon–Sulphur Cathode for Lithium–Sulphur Batteries. *Nat. Mater.* **2009**, *8* (6), 500–506. https://doi.org/10.1038/nmat2460.

(8) Crossland, E. J. W.; Kamperman, M.; Nedelcu, M.; Ducati, C.; Wiesner, U.; Smilgies, D.-M.; Toombes, G. E. S.; Hillmyer, M. A.; Ludwigs, S.; Steiner, U.; Snaith, H. J. A Bicontinuous Double Gyroid Hybrid Solar Cell. *Nano Lett.* **2009**, *9* (8), 2807–2812. https://doi.org/10.1021/nl803174p.

(9) Tan, K. W.; Moore, D. T.; Saliba, M.; Sai, H.; Estroff, L. A.; Hanrath, T.; Snaith, H. J.; Wiesner, U. Thermally Induced Structural Evolution and Performance of Mesoporous Block Copolymer-Directed Alumina Perovskite Solar Cells. *ACS Nano* **2014**, *8* (5), 4730–4739. https://doi.org/10.1021/nn500526t.

(10) Saliba, M.; Tan, K. W.; Sai, H.; Moore, D. T.; Scott, T.; Zhang, W.; Estroff, L. A.; Wiesner, U.; Snaith, H. J. Influence of Thermal Processing Protocol upon the Crystallization and Photovoltaic Performance of Organic–Inorganic Lead Trihalide Perovskites. *J. Phys. Chem. C* **2014**, *118* (30), 17171–17177. https://doi.org/10.1021/jp500717w.

(11) Wang, L.; Seah, G. L.; Li, Y.; Tu, W. H.; Manalastas Jr., W.; Reavley, M. J.-H.; Corcoran Jr., E. W.; Usadi, A. K.; Du, Z.; Madhavi, S.; McConnachie, J. M.; Ong, H. G.; Tan, K. W. Ultrafast Crystallization of Ordered Mesoporous Metal Oxides and Carbon from Block Copolymer Self-Assembly and Joule Heating. *Adv. Mater. Interfaces* **2022**, *9* (19), 2200151. https://doi.org/10.1002/admi.202200151.

(12) Vallet-Regi, M.; Rámila, A.; del Real, R. P.; Pérez-Pariente, J. A New Property of MCM-41: Drug Delivery System. *Chem. Mater.* **2001**, *13* (2), 308–311. https://doi.org/10.1021/cm0011559.

(13) Suteewong, T.; Sai, H.; Cohen, R.; Wang, S.; Bradbury, M.; Baird, B.; Gruner, S. M.; Wiesner, U. Highly Aminated Mesoporous Silica Nanoparticles with Cubic Pore Structure. *J. Am. Chem. Soc.* **2011**, *133* (2), 172–175. https://doi.org/10.1021/ja1061664.
(14) Wu, S.-H.; Hung, Y.; Mou, C.-Y. Mesoporous Silica Nanoparticles as Nanocarriers. *Chem. Commun.* **2011**, *47* (36), 9972. https://doi.org/10.1039/c1cc11760b.
(15) Chen, Y.; Chen, H.; Shi, J. In Vivo Bio-Safety Evaluations and Diagnostic/Therapeutic Applications of Chemically Designed Mesoporous Silica Nanoparticles. *Adv. Mater.* **2013**, *25* (23), 3144–3176. https://doi.org/10.1002/adma.201205292.
(16) Hao, N.; Jayawardana, K. W.; Chen, X.; Yan, M. One-Step Synthesis of Amine-Functionalized Hollow Mesoporous Silica Nanoparticles as Efficient Antibacterial and Anticancer Materials. *ACS Appl. Mater. Interfaces* **2015**, *7* (2), 1040–1045. https://doi.org/10.1021/am508219g.
(17) Lim, H. K.; Tan, S. J.; Wu, Z.; Ong, B. C.; Tan, K. W.; Dong, Z.; Tay, C. Y. Diatom-Inspired 2D Nitric Oxide Releasing Anti-Infective Porous Nanofrustules. *J. Mater. Chem. B* **2021**, *9* (35), 7229–7237. https://doi.org/10.1039/D1TB00458A.
(18) Xi, L.; Zhang, M.; Zhang, L.; Lew, T. T. S.; Lam, Y. M. Novel Materials for Urban Farming. *Adv. Mater.* **2021**, 2105009. https://doi.org/10.1002/adma.202105009.
(19) Black, C. T.; Guarini, K. W.; Milkove, K. R.; Baker, S. M.; Russell, T. P.; Tuominen, M. T. Integration of Self-Assembled Diblock Copolymers for Semiconductor Capacitor Fabrication. *Appl. Phys. Lett.* **2001**, *79* (3), 409–411. https://doi.org/10.1063/1.1383805.
(20) Arora, H.; Du, P.; Tan, K. W.; Hyun, J. K.; Grazul, J.; Xin, H. L.; Muller, D. A.; Thompson, M. O.; Wiesner, U. Block Copolymer Self-Assembly–Directed Single-Crystal Homo- and Heteroepitaxial Nanostructures. *Science* **2010**, *330* (6001), 214–219. https://doi.org/10.1126/science.1193369.
(21) Tan, K. W.; Jung, B.; Werner, J. G.; Rhoades, E. R.; Thompson, M. O.; Wiesner, U. Transient Laser Heating Induced Hierarchical Porous Structures from Block Copolymer–Directed Self-Assembly. *Science* **2015**, *349* (6243), 54–58. https://doi.org/10.1126/science.aab0492.
(22) Stöber, W.; Fink, A.; Bohn, E. Controlled Growth of Monodisperse Silica Spheres in the Micron Size Range. *J. Colloid Interface Sci.* **1968**, *26* (1), 62–69. https://doi.org/10.1016/0021-9797(68)90272-5.
(23) Brinker, C. Jeffrey.; Scherer, G. W. *Sol-Gel Science: The Physics and Chemistry of Sol-Gel Processing*; Academic Press: Boston, 1990.
(24) Yanagisawa, T.; Shimizu, T.; Kuroda, K.; Kato, C. The Preparation of Alkyltriinethylaininonium–Kaneinite Complexes and Their Conversion to Microporous Materials. *Bull. Chem. Soc. Jpn.* **1990**, *63* (4), 988–992. https://doi.org/10.1246/bcsj.63.988.
(25) Kresge, C. T.; Leonowicz, M. E.; Roth, W. J.; Vartuli, J. C.; Beck, J. S. Ordered Mesoporous Molecular Sieves Synthesized by a Liquid-Crystal Template Mechanism. *Nature* **1992**, *359* (6397), 710–712. https://doi.org/10.1038/359710a0.
(26) Huo, Q.; Leon, R.; Petroff, P. M.; Stucky, G. D. Mesostructure Design with Gemini Surfactants: Supercage Formation in a Three-Dimensional Hexagonal Array. *Science* **1995**, *268* (5215), 1324–1327. https://doi.org/10.1126/science.268.5215.1324.
(27) Templin, M.; Franck, A.; Chesne, A. D.; Leist, H.; Zhang, Y.; Ulrich, R.; Schädler, V.; Wiesner, U. Organically Modified Aluminosilicate Mesostructures from Block Copolymer Phases. *Science* **1997**, *278* (5344), 1795–1798. https://doi.org/10.1126/science.278.5344.1795.

(28) Zhao, D.; Feng, J.; Huo, Q.; Melosh, N.; Fredrickson, G. H.; Chmelka, B. F.; Stucky, G. D. Triblock Copolymer Syntheses of Mesoporous Silica with Periodic 50 to 300 Angstrom Pores. *Science* **1998**, *279* (5350), 548–552. https://doi.org/10.1126/science.279.5350.548.
(29) Kleitz, F.; Choi, S. H.; Ryoo, R. Cubic *Ia*3*d* Large Mesoporous Silica: Synthesis and Replication to Platinum Nanowires, Carbon Nanorods and Carbon Nanotubes. *Chem. Commun.* **2003**, No. 17, 2136–2137. https://doi.org/10.1039/B306504A.
(30) Che, S.; Liu, Z.; Ohsuna, T.; Sakamoto, K.; Terasaki, O.; Tatsumi, T. Synthesis and Characterization of Chiral Mesoporous Silica. *Nature* **2004**, *429* (6989), 281–284. https://doi.org/10.1038/nature02529.
(31) Xiao, C.; Fujita, N.; Miyasaka, K.; Sakamoto, Y.; Terasaki, O. Dodecagonal Tiling in Mesoporous Silica. *Nature* **2012**, *487* (7407), 349–353. https://doi.org/10.1038/nature11230.
(32) Suteewong, T.; Sai, H.; Hovden, R.; Muller, D.; Bradbury, M. S.; Gruner, S. M.; Wiesner, U. Multicompartment Mesoporous Silica Nanoparticles with Branched Shapes: An Epitaxial Growth Mechanism. *Science* **2013**, *340* (6130), 337–341. https://doi.org/10.1126/science.1231391.
(33) Suteewong, T.; Sai, H.; Bradbury, M.; Estroff, L. A.; Gruner, S. M.; Wiesner, U. Synthesis and Formation Mechanism of Aminated Mesoporous Silica Nanoparticles. *Chem. Mater.* **2012**, *24* (20), 3895–3905. https://doi.org/10.1021/cm301857e.
(34) Sun, Y.; Sai, H.; Spoth, K. A.; Tan, K. W.; Werner-Zwanziger, U.; Zwanziger, J.; Gruner, S. M.; Kourkoutis, L. F.; Wiesner, U. Stimuli-Responsive Shapeshifting Mesoporous Silica Nanoparticles. *Nano Lett.* **2016**, *16* (1), 651–655. https://doi.org/10.1021/acs.nanolett.5b04395.
(35) Sun, Y.; Ma, K.; Kao, T.; Spoth, K. A.; Sai, H.; Zhang, D.; Kourkoutis, L. F.; Elser, V.; Wiesner, U. Formation Pathways of Mesoporous Silica Nanoparticles with Dodecagonal Tiling. *Nat. Commun.* **2017**, *8* (1), 252. https://doi.org/10.1038/s41467-017-00351-8.
(36) Ma, K.; Gong, Y.; Aubert, T.; Turker, M. Z.; Kao, T.; Doerschuk, P. C.; Wiesner, U. Self-Assembly of Highly Symmetrical, Ultrasmall Inorganic Cages Directed by Surfactant Micelles. *Nature* **2018**, *558* (7711), 577–580. https://doi.org/10.1038/s41586-018-0221-0.
(37) Aubert, T.; Ma, K.; Tan, K. W.; Wiesner, U. Two-Dimensional Superstructures of Silica Cages. *Adv. Mater.* **2020**, *32* (21), 1908362. https://doi.org/10.1002/adma.201908362.
(38) Chen, Q.; Han, L.; Gao, C.; Che, S. Synthesis of Monodispersed Mesoporous Silica Spheres (MMSSs) with Controlled Particle Size Using Gemini Surfactant. *Microporous Mesoporous Mater.* **2010**, *128* (1), 203–212. https://doi.org/10.1016/j.micromeso.2009.08.024.
(39) Li, M.; Zhang, C.; Yang, X. Gemini Surfactants Templated Mesoporous Silica Microparticles: From Solid to Hollow Mesoporous Spheres. *Chin. J. Chem.* **2017**, *35* (11), 1706–1710. https://doi.org/10.1002/cjoc.201700277.
(40) Ratirotjanakul, W.; Suteewong, T.; Polpanich, D.; Tangboriboonrat, P. Amino Acid as a Biodegradation Accelerator of Mesoporous Silica Nanoparticles. *Microporous Mesoporous Mater.* **2019**, *282*, 243–251. https://doi.org/10.1016/j.micromeso.2019.02.033.
(41) Suteewong, T.; Ma, K.; Drews, J. E.; Werner-Zwanziger, U.; Zwanziger, J.; Wiesner, U.; Bradbury, M. S. Highly Fluorescent Sub 40-Nm Aminated Mesoporous Silica Nanoparticles. *J. Sol-Gel Sci. Technol.* **2015**, *74* (1), 32–38. https://doi.org/10.1007/s10971-014-3567-2.

(42) Joo, S. H.; Choi, S. J.; Oh, I.; Kwak, J.; Liu, Z.; Terasaki, O.; Ryoo, R. Ordered Nanoporous Arrays of Carbon Supporting High Dispersions of Platinum Nanoparticles. *Nature* **2001**, *412* (6843), 169–172. https://doi.org/10.1038/35084046.
(43) Tan, K. W.; Saba, S. A.; Arora, H.; Thompson, M. O.; Wiesner, U. Colloidal Self-Assembly-Directed Laser-Induced Non-Close-Packed Crystalline Silicon Nanostructures. *ACS Nano* **2011**, *5* (10), 7960–7966. https://doi.org/10.1021/nn2023446.
(44) Wu, S.-H.; Mou, C.-Y.; Lin, H.-P. Synthesis of Mesoporous Silica Nanoparticles. *Chem. Soc. Rev.* **2013**, *42* (9), 3862–3875. https://doi.org/10.1039/C3CS35405A.
(45) Kankala, R. K.; Han, Y.-H.; Na, J.; Lee, C.-H.; Sun, Z.; Wang, S.-B.; Kimura, T.; Ok, Y. S.; Yamauchi, Y.; Chen, A.-Z.; Wu, K. C.-W. Nanoarchitectured Structure and Surface Biofunctionality of Mesoporous Silica Nanoparticles. *Adv. Mater.* **2020**, *32* (23), 1907035. https://doi.org/10.1002/adma.201907035.
(46) Li, X.; Zhou, L.; Wei, Y.; El-Toni, A. M.; Zhang, F.; Zhao, D. Anisotropic Growth-Induced Synthesis of Dual-Compartment Janus Mesoporous Silica Nanoparticles for Bimodal Triggered Drugs Delivery. *J. Am. Chem. Soc.* **2014**, *136* (42), 15086–15092. https://doi.org/10.1021/ja508733r.
(47) Li, X.; Zhou, L.; Wei, Y.; El-Toni, A. M.; Zhang, F.; Zhao, D. Anisotropic Encapsulation-Induced Synthesis of Asymmetric Single-Hole Mesoporous Nanocages. *J. Am. Chem. Soc.* **2015**, *137* (18), 5903–5906. https://doi.org/10.1021/jacs.5b03207.
(48) Zhang, K.; Xu, L.-L.; Jiang, J.-G.; Calin, N.; Lam, K.-F.; Zhang, S.-J.; Wu, H.-H.; Wu, G.-D.; Albela, B.; Bonneviot, L.; Wu, P. Facile Large-Scale Synthesis of Monodisperse Mesoporous Silica Nanospheres with Tunable Pore Structure. *J. Am. Chem. Soc.* **2013**, *135* (7), 2427–2430. https://doi.org/10.1021/ja3116873.
(49) Wei, J.; Yue, Q.; Sun, Z.; Deng, Y.; Zhao, D. Synthesis of Dual-Mesoporous Silica Using Non-Ionic Diblock Copolymer and Cationic Surfactant as Co-Templates. *Angew. Chem., Int. Ed.* **2012**, *51* (25), 6149–6153. https://doi.org/10.1002/anie.201202232.
(50) Hao, N.; Nie, Y.; Zhang, J. X. J. Biomimetic Hierarchical Walnut Kernel-like and Erythrocyte-like Mesoporous Silica Nanomaterials: Controllable Synthesis and Versatile Applications. *Microporous Mesoporous Mater.* **2018**, *261*, 144–149. https://doi.org/10.1016/j.micromeso.2017.11.003.
(51) Chen, F.; Hong, H.; Shi, S.; Goel, S.; Valdovinos, H. F.; Hernandez, R.; Theuer, C. P.; Barnhart, T. E.; Cai, W. Engineering of Hollow Mesoporous Silica Nanoparticles for Remarkably Enhanced Tumor Active Targeting Efficacy. *Sci. Rep.* **2014**, *4* (1), 5080. https://doi.org/10.1038/srep05080.
(52) Li, Y.; Li, N.; Pan, W.; Yu, Z.; Yang, L.; Tang, B. Hollow Mesoporous Silica Nanoparticles with Tunable Structures for Controlled Drug Delivery. *ACS Appl. Mater. Interfaces* **2017**, *9* (3), 2123–2129. https://doi.org/10.1021/acsami.6b13876.
(53) Albanese, A.; Tang, P. S.; Chan, W. C. W. The Effect of Nanoparticle Size, Shape, and Surface Chemistry on Biological Systems. *Annu. Rev. Biomed. Eng.* **2012**, *14* (1), 1–16. https://doi.org/10.1146/annurev-bioeng-071811-150124.
(54) Li, M.; Zhang, C.; Yang, X.-L.; Xu, H.-B. Controllable Synthesis of Hollow Mesoporous Silica Nanoparticles Templated by Kinetic Self-Assembly Using a Gemini Surfactant. *RSC Adv.* **2013**, *3* (37), 16304. https://doi.org/10.1039/c3ra22805c.
(55) Menger, F. M.; Keiper, J. S. Gemini Surfactants. *Angew. Chem., Int. Ed.* **2000**, *39* (11), 1906–1920. https://doi.org/10.1002/1521-3773(20000602)39:11<1906::AID-ANIE1906>3.0.CO;2-Q.

(56) In, M.; Zana, R. Phase Behavior of Gemini Surfactants. *J. Dispersion Sci. Technol.* **2007**, *28* (1), 143–154. https://doi.org/10.1080/01932690600991888.
(57) Aswal, V. K.; De, S.; Goyal, P. S.; Bhattacharya, S.; Heenan, R. K. Transition from Disc to Rod-like Shape of 16-3-16 Dimeric Micelles in Aqueous Solutions. *J. Chem. Soc., Faraday Trans.* **1998**, *94* (19), 2965–2967. https://doi.org/10.1039/A805307C.
(58) Yi, Z.; Dumée, L. F.; Garvey, C. J.; Feng, C.; She, F.; Rookes, J. E.; Mudie, S.; Cahill, D. M.; Kong, L. A New Insight into Growth Mechanism and Kinetics of Mesoporous Silica Nanoparticles by in Situ Small Angle X-Ray Scattering. *Langmuir* **2015**, *31* (30), 8478–8487. https://doi.org/10.1021/acs.langmuir.5b01637.
(59) Kimura, T.; Itoh, D.; Shigeno, T.; Kuroda, K. Silica-Based Mesostructured Materials Induced by Surfactant Assemblies in the Two-Dimensionally Limited Space of a Layered Polysilicate Kanemite. *Bull. Chem. Soc. Jpn.* **2004**, *77* (3), 585–590. https://doi.org/10.1246/bcsj.77.585.
(60) Atluri, R.; Sakamoto, Y.; Garcia-Bennett, A. E. Co-Structure Directing Agent Induced Phase Transformation of Mesoporous Materials. *Langmuir* **2009**, *25* (5), 3189–3195. https://doi.org/10.1021/la803727u.
(61) Ma, C.; Han, L.; Jiang, Z.; Huang, Z.; Feng, J.; Yao, Y.; Che, S. Growth of Mesoporous Silica Film with Vertical Channels on Substrate Using Gemini Surfactants. *Chem. Mater.* **2011**, *23* (16), 3583–3586. https://doi.org/10.1021/cm201356n.
(62) Huo, Q.; Margolese, D. I.; Ciesla, U.; Feng, P.; Gier, T. E.; Sieger, P.; Leon, R.; Petroff, P. M.; Schüth, F.; Stucky, G. D. Generalized Synthesis of Periodic Surfactant/Inorganic Composite Materials. *Nature* **1994**, *368* (6469), 317–321. https://doi.org/10.1038/368317a0.
(63) Wan, Y.; Zhao. On the Controllable Soft-Templating Approach to Mesoporous Silicates. *Chem. Rev.* **2007**, *107* (7), 2821–2860. https://doi.org/10.1021/cr068020s.
(64) Che, S.; Garcia-Bennett, A. E.; Yokoi, T.; Sakamoto, K.; Kunieda, H.; Terasaki, O.; Tatsumi, T. A Novel Anionic Surfactant Templating Route for Synthesizing Mesoporous Silica with Unique Structure. *Nat. Mater.* **2003**, *2* (12), 801–805. https://doi.org/10.1038/nmat1022.
(65) Huh, S.; Wiench, J. W.; Yoo, J.-C.; Pruski, M.; Lin, V. S.-Y. Organic Functionalization and Morphology Control of Mesoporous Silicas via a Co-Condensation Synthesis Method. *Chem. Mater.* **2003**, *15* (22), 4247–4256. https://doi.org/10.1021/cm0210041.
(66) Cölfen, H.; Antonietti, M. Mesocrystals: Inorganic Superstructures Made by Highly Parallel Crystallization and Controlled Alignment. *Angew. Chem., Int. Ed.* **2005**, *44* (35), 5576–5591. https://doi.org/10.1002/anie.200500496.
(67) Hajipour, M. J.; Fromm, K. M.; Ashkarran, A. A.; Aberasturi, D. J. de; Larramendi, I. R. de; Rojo, T.; Serpooshan, V.; Parak, W. J.; Mahmoudi, M. Antibacterial Properties of Nanoparticles. *Trends Biotechnol.* **2012**, *30* (10), 499–511. https://doi.org/10.1016/j.tibtech.2012.06.004.
(68) Frattini, A.; Pellegri, N.; Nicastro, D.; Sanctis, O. de. Effect of Amine Groups in the Synthesis of Ag Nanoparticles Using Aminosilanes. *Mater. Chem. Phys.* **2005**, *94* (1), 148–152. https://doi.org/10.1016/j.matchemphys.2005.04.023.
(69) Wongpreecha, J.; Polpanich, D.; Suteewong, T.; Kaewsaneha, C.; Tangboriboonrat, P. One-Pot, Large-Scale Green Synthesis of Silver Nanoparticles-Chitosan with Enhanced Antibacterial Activity and Low Cytotoxicity. *Carbohydr. Polym* **2018**, *199*, 641–648. https://doi.org/10.1016/j.carbpol.2018.07.039.

(70) Zhou, L.; Fan, J.; Cui, G.; Shang, X.; Tang, Q.; Wang, J.; Fan, M. Highly Efficient and Reversible CO_2 Adsorption by Amine-Grafted Platelet SBA-15 with Expanded Pore Diameters and Short Mesochannels. *Green Chem.* **2014**, *16* (8), 4009–4016. https://doi.org/10.1039/C4GC00832D.
(71) Watabe, T.; Yogo, K. Isotherms and Isosteric Heats of Adsorption for CO2 in Amine-Functionalized Mesoporous Silicas. *Sep. Purif. Technol.* **2013**, *120*, 20–23. https://doi.org/10.1016/j.seppur.2013.09.011.
(72) Liu, Q.; Shi, J.; Zheng, S.; Tao, M.; He, Y.; Shi, Y. Kinetics Studies of CO_2 Adsorption/Desorption on Amine-Functionalized Multiwalled Carbon Nanotubes. *Ind. Eng. Chem. Res.* **2014**, *53* (29), 11677–11683. https://doi.org/10.1021/ie502009n.
(73) Ho, Y. S.; McKay, G. Pseudo-Second Order Model for Sorption Processes. *Process Biochem.* **1999**, *34* (5), 451–465. https://doi.org/10.1016/S0032-9592(98)00112-5.
(74) Zana, R.; Benrraou, M.; Rueff, R. Alkanediyl-.Alpha.,.Omega.-Bis(Dimethylalkylammonium Bromide) Surfactants. 1. Effect of the Spacer Chain Length on the Critical Micelle Concentration and Micelle Ionization Degree. *Langmuir* **1991**, *7* (6), 1072–1075. https://doi.org/10.1021/la00054a008.
(75) Brunauer, S.; Emmett, P. H.; Teller, E. Adsorption of Gases in Multimolecular Layers. *J. Am. Chem. Soc.* **1938**, *60* (2), 309–319. https://doi.org/10.1021/ja01269a023.
(76) Barrett, E. P.; Joyner, L. G.; Halenda, P. P. The Determination of Pore Volume and Area Distributions in Porous Substances. I. Computations from Nitrogen Isotherms. *J. Am. Chem. Soc.* **1951**, *73* (1), 373–380. https://doi.org/10.1021/ja01145a126.